3D SAR BEAMFORMING UNDER A FOLIAGE CANOPY FROM A SINGLE PASS

P.B. Pincus†, M. Preiss**

**Defence Science & Technology Organisation
Edinburgh, SA, Australia*

D.A. Gray†

†University of Adelaide Radar Research Centre
School of EEE, U. Adelaide, SA, Australia

ABSTRACT

Coherent detection of changes on the ground under a forest canopy by repeat-pass synthetic aperture radar (SAR) imaging is problematic due to the mixture of ground and canopy responses. 3D SAR imaging, by beamforming data from multiple low-frequency across-track acquisitions, offers a way to separate the forest components in height. However, data acquired from multiple passes require precise registration of the flight tracks, which is often not possible, particularly for small airborne platforms. This study analyses the potential for SAR imaging of the ground under a forest canopy using data from a single pass of a multichannel across-track radar system. We focus in particular on the case of a two-channel alternating-transmit interferometer giving three effective input channels. 3D image formation in one pass by phase-preserving adaptive beamforming is shown to provide sufficient attenuation of the interference from a model forest volume to permit a reasonable estimation of the ground coherence across two passes for coherent change detection.

Index Terms— 3D SAR, beamforming, interferometry

1. INTRODUCTION

Synthetic aperture radar imaging is a mature remote-sensing technology which produces 2D maps of the complex reflectivity of the Earth's surface. The coherent difference between two image channels permits the extraction of topographic or change information, depending on the separation of the channels in incidence angle and/or time [1, 2]. Vertical resolution is achieved by coherently synthesising an aperture from multiple SAR image channels acquired at different incidence angles. This aperture synthesis is typically cast as a beamforming task, where the acquisition positions form an array and input 2D SAR images are weighted and summed to form 3D SAR images focused to different heights; this effectively scans beams in height [3]. There has been significant interest in applying 3D SAR to the remote sensing of forests, where a foliage-penetrating radar wavelength allows the vertical structure to be coarsely estimated [4].

Past demonstrations of 3D SAR have generally involved several repeat passes of a radar platform at different altitudes or standoffs [5, 6]. This is a significant data collection burden, and it greatly increases the scope for motion compensation errors which in beamforming terms are errors in the array manifold. In addition, the imaged scene may change during collection. Acquisition in a single pass would avoid these deficiences. Current interferometric radars use two antennas offset in an across-track sense i.e. they observe the scene at slightly different incidence angles, transmitting pulses alternately on each antenna and receiving on both [7, 8]. This alternating operation gives rise to three effective phase centres, following the principles of bistatic radar [9] – see Fig. 1. Historically, such a mode has been considered in terms of improving the interferometric estimate of topography [10], but recently it has been demonstrated that this mode enables coarse 3D SAR image formation [11, 12].

In this study we seek to first image the ground under a forest canopy by beamforming the data from a single-pass of a multichannel across-track radar system, and then coherently detect changes on the ground by correlating two such images acquired at different times from repeat passes. Modern change detection algorithms require an accurate estimate of the repeat-pass coherence. The above-ground forest acts as volumetric interference which distorts the coherence of the ground response. We decompose the scene coherence and show that, in forming a 3D image focused to the ground, a beamformer attenuates the volume component. Moreover, we demonstrate that standard adaptive beamforming (a.k.a. minimum variance distortionless response (MVDR)), which forms phase-preserved 3D images, attenuates the volume sufficiently to permit accurate estimation of the ground coherence, given a simple model of a forest canopy as a random volume. The novel contribution of this work is an analysis of coherent change detection under a forest canopy using 3D SAR images generated from very limited data, in particular, three channels from a single pass.

2. 3D SAR IMAGE FORMATION

Consider a single pass of a radar platform with P physical antennas uniformly spaced in the across-track direction. If pulse transmission alternates between the two edge antennas, but all antennas receive each pulse, then $N = 2P - 1$ effective phase centres will be synthesised, giving N 2D SAR images. The common case of $N = 3$ is shown in Fig. 1.

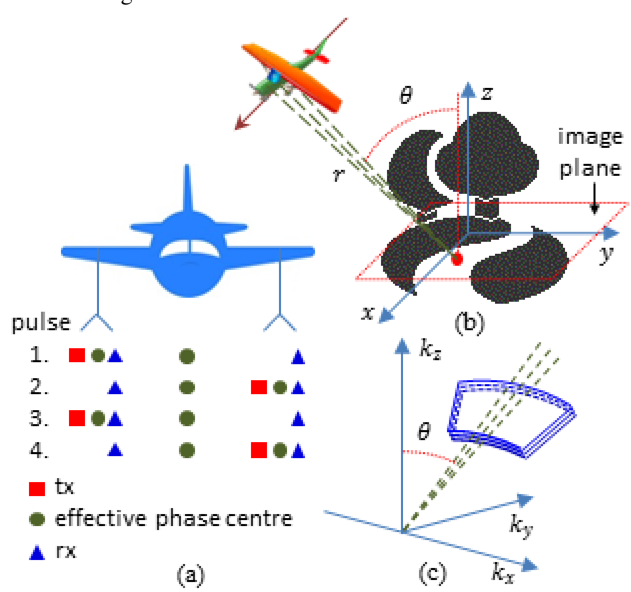

Fig. 1. (a) Airborne example of $P = 2$ physical antennas giving $N = 3$ effective phase centres. (b) Cylindrical coordinates denote the position (x_n, r_n, θ_n) of the acquisition channels $n = 1, 2...N$ relative to a position (x, y, z) in the scene. (c) The associated bandwidth support in the spatial-frequency domain. The radial offset to the centre of each spectral region is $k_0 = 4\pi/\lambda$.

For simplicity, assume broadside imaging $x_n = 0$ so that the azimuth coordinate x can be suppressed. Consider a single position (y, z). Each input 2D image contributes a pixel estimate $p_n = \hat{f}_n(r_n) \exp(j\phi_n)$ of the complex reflectivity $f(y, z)$, where $\phi_n = k_0 r_n = 4\pi r_n/\lambda$ is the phase due to propagation of the signal. The estimate is unresolved in incidence angle θ and may contain contributions from various positions $(r_n \sin\theta, r_n \cos\theta)$ along an iso-range contour. After calibration and coregistration, the N estimates fill the array sample vector $\mathbf{x} = [p_n]$. The steering vector $\mathbf{v} = [\exp(j\phi_n)]$ associated with (y, z) contains the propagation phases for the collection geometry of each channel (these may be made relative to one channel). For distributed clutter, the reflectivity estimates will exhibit a statistical variation due to speckle [3].

A 3D SAR image may be formed by combining the channel estimates into a new estimate of the complex reflectivity $\hat{f}(y, z) = \mathbf{w}^H \mathbf{x}$, where the range-dependent phases $\mathbf{w}$ steer beams to resolve scatterers in height. Weight selection is a standard beamforming problem; we consider it in terms of the coherence between two 3D images.

3. TWO-PASS MULTICHANNEL COHERENCE

Two passes, a and b, of the radar platform will provide two 3D images, $\hat{f}_a = \mathbf{w}_a^H \mathbf{x}_a$ and $\hat{f}_b = \mathbf{w}_b^H \mathbf{x}_b$. Differences in the scene can be measured by the images' coherence γ_{ab} [2].

$$\gamma_{ab} = \frac{\mathrm{E}\{\hat{f}_a \hat{f}_b^*\}}{\sqrt{\mathrm{E}\{\hat{f}_a \hat{f}_a^*\}\mathrm{E}\{\hat{f}_b \hat{f}_b^*\}}} = \frac{\mathbf{w}_a^H R_{ab} \mathbf{w}_b}{\sqrt{\mathbf{w}_a^H R_a \mathbf{w}_a \mathbf{w}_b^H R_b \mathbf{w}_b}} \tag{1}$$

where element (m, n) of the covariance matrices $R_a = \mathrm{E}\{\mathbf{x}_a \mathbf{x}_a^H\}$ and $R_b = \mathrm{E}\{\mathbf{x}_b \mathbf{x}_b^H\}$ is the correlation between channels m and n within pass a and pass b, respectively, whereas the cross-covariance matrix $R_{ab} = \mathrm{E}\{\mathbf{x}_a \mathbf{x}_b^H\}$ contains the correlations between channels across the passes i.e. channel m is from pass a and channel n is from pass b. While the covariance-matrix expression in (1) is used in this paper for analysing γ_{ab}, data processing would involve forming the two 3D images via beamforming and computing their coherence.

Assume that the mean power σ^2 received in all channels is the same. Within a pass, this is reasonable because the antennas view the scene simultaneously at similar geometries. Across passes, this is a stronger assumption, but is commonly observed where the scene changes are subtle changes in the speckle pattern [2], and it is these changes we wish to detect. This allows each covariance matrix to be treated as a scaled matrix of channel coherences i.e. $R = \sigma^2[\gamma^{(mn)}]$. Note that σ^2 will cancel out from the total coherence in (1).

4. TWO-LAYER FOREST MODEL

The coherence between any channel pair (m, n) from either the same pass or different passes may be decomposed according to a simple two-layer model of a forest scene as a dense volume v over a ground surface g, plus noise q, in order to identify the desired ground component and analyse how it is perturbed.

Let distinct observations x_m and x_n each consist of independent ground, volume and noise components. The ground and volume components can each be further divided into a part which is correlated (c) across the images, and parts which are uncorrelated (d) but assumed to have the same average power [13].

$$x_m = c_g + d_{g_m} + c_v + d_{v_m} + q_m \tag{2}$$

$$x_n = c_g e^{j\phi_g} + d_{g_n} + c_v e^{j\phi_v} + d_{v_n} + q_n \tag{3}$$

We have slightly extended Zebker and Villasenor's derivation [13] by allowing for phase differences ϕ_g and ϕ_v between the correlated components, which may arise due to uncompensated differences in the propagation distances to the scatterers – this difference is the basis for topographic mapping by interferometry [1]. The noises are uncorrelated but assumed to have equal power.

The coherence can be decomposed as a product where each factor contains the decorrelation due to a single source. Further rearrangement yields the coherence of each source in isolation, the power ratio between sources, and the SNR.

$$\begin{aligned}\gamma^{(mn)} &= \frac{\mathrm{E}\{x_n x_m^*\}}{\sqrt{\mathrm{E}\{x_m x_m^*\}\mathrm{E}\{x_n x_n^*\}}} \\ &= \frac{\sigma_{c_g}^2 e^{j\phi_g} + \sigma_{c_v}^2 e^{j\phi_v}}{\sigma_{c_g}^2 + \sigma_{c_v}^2 + \sigma_{d_g}^2 + \sigma_{d_v}^2 + \sigma_q^2} = \tilde{\gamma}_g \tilde{\gamma}_v \gamma_{SNR}\end{aligned} \tag{4}$$

where

$$\tilde{\gamma}_g = \frac{\sigma_{c_g}^2 e^{j\phi_g} + \sigma_{c_v}^2 e^{j\phi_v}}{\sigma_{c_g}^2 + \sigma_{c_v}^2 e^{j\phi_v} + \sigma_{d_g}^2} = \frac{\gamma_g + \gamma_v/\mu}{1 + \gamma_v/\mu} \tag{5}$$

$$\tilde{\gamma}_v = \frac{\sigma_{c_g}^2 + \sigma_{c_v}^2 e^{j\phi_v} + \sigma_{d_g}^2}{\sigma_{c_g}^2 + \sigma_{c_v}^2 + \sigma_{d_g}^2 + \sigma_{d_v}^2} = \frac{\gamma_v + \mu}{1 + \mu} \tag{6}$$

$$\gamma_{SNR} = \frac{\sigma_{c_g}^2 + \sigma_{c_v}^2 + \sigma_{d_g}^2 + \sigma_{d_v}^2}{\sigma_{c_g}^2 + \sigma_{c_v}^2 + \sigma_{d_g}^2 + \sigma_{d_v}^2 + \sigma_q^2} = \frac{1}{1 + SNR^{-1}}$$

and setting $\sigma_g^2 = \sigma_{c_g}^2 + \sigma_{d_g}^2$ and $\sigma_v^2 = \sigma_{c_v}^2 + \sigma_{d_v}^2$ ($\sigma^2 = \sigma_g^2 + \sigma_v^2 + \sigma_q^2$),

$$\begin{aligned}\gamma_g &= (\sigma_{c_g}^2/\sigma_g^2) e^{j\phi_g} && \text{(ground-only coherence)} \\ \gamma_v &= (\sigma_{c_v}^2/\sigma_v^2) e^{j\phi_v} && \text{(volume-only coherence)} \\ \mu &= \sigma_g^2/\sigma_v^2 && \text{(ground/volume power ratio)} \\ SNR &= (\sigma_g^2 + \sigma_v^2)/\sigma_q^2. &&\end{aligned}$$

The layer components combine as a weighted sum

$$\tilde{\gamma}_{gv} \triangleq \tilde{\gamma}_g \tilde{\gamma}_v = \frac{\gamma_g + \gamma_v/\mu}{1 + 1/\mu} = \frac{\mu}{1 + \mu}\gamma_g + \frac{1}{1 + \mu}\gamma_v. \tag{7}$$

The magnitude of the ground-only coherence γ_g is the parameter we wish to recover as a coherent change map across passes, but it is distorted by the volume-only coherence γ_v, the finite ground/volume power ratio μ and the noise.

5. MULTICHANNEL VOLUME ATTENUATION

In general, the decomposition in (2)-(3) is unique to each channel pair. Each coherence term will depend on the relative collection geometry of the pair and the scene reflectivity at the times of acquisition. However, for typical single-pass multichannel radar platforms and typical repeat-passes for change detection, the difference in incidence angles $\Delta\theta_{mn}$ between any channel pair (m, n) is small (see Fig. 1), and for typical foliage-penetrating wavelengths, the consequent geometric decorrelation of surface scatter will be small too. (Filtering of the spatial frequencies can reduce this if needed [14].) If the ground topography is known, the 2D images can be focused to the ground surface, such that $\phi_g = 0$ [15]. The scene itself is constant within a pass. Therefore, the ground coherence is approximately unity within a pass, and a constant γ_{ab_g} across passes. Additionally, assume that the ground, volume and noise component powers are constants across channels and passes, and for simplicity, assume that the decorrelation due to noise is negligible because the SNR after coherent image formation is high. Therefore, using (4) and (7), the covariance matrices in (1) reduce to

$$R_a = \sigma^2 \left(\frac{\mu}{1 + \mu}\mathbf{1}_{N\times N} + \frac{1}{1 + \mu}R_{a_v}\right) \tag{8}$$

$$R_{ab} = \sigma^2 \left(\frac{\mu}{1 + \mu}\mathbf{1}_{N\times N}\gamma_{ab_g} + \frac{1}{1 + \mu}R_{ab_v}\right) \tag{9}$$

where $R_{a_v} = \left[\gamma_{a_v}^{(mn)}\right]$ and $R_{ab_v} = \left[\gamma_{ab_v}^{(mn)}\right]$. R_b mirrors R_a.

The volume coherences are strongly dependent on $\Delta\theta_{mn}$, so the covariance matrices will generally have full rank. A finite-bandwidth sensor can resolve a dense scene only in the sense of evaluating the net response in a small volume observed from a particular angle. This distributed-target characteristic of natural landscapes stands in contrast to radar observation of identifiable and coherent sources.

Consider the simple case when the collection geometries are similar for the two passes and the forest volume is effectively constant, not unreasonable for a long wavelength and short time-scale. Therefore, corresponding coherences within the two passes will be approximately equal i.e. $R_{a_v}\approx R_{b_v}$, $R_a\approx R_b$ and $\mathbf{w}_a\approx\mathbf{w}_b$.

Substituting (8) and (9) into (1), the total coherence is simply

$$\gamma_{ab} = \frac{\mathbf{w}_a^H R_{ab}\mathbf{w}_a}{\mathbf{w}_a^H R_a \mathbf{w}_a} = \frac{\gamma_{ab_g} + \beta_v\alpha_v/\mu}{1+\alpha_v/\mu} = \hat{\gamma}_{ab_g} \quad (10)$$

where

$$\alpha_v = \frac{\mathbf{w}_a^H R_{a_v}\mathbf{w}_a}{\mathbf{w}_a^H \mathbf{1}_{N\times N}\mathbf{w}_a} \qquad (0<\alpha_v<1) \quad (11)$$

$$\beta_v = \frac{\mathbf{w}_a^H R_{ab_v}\mathbf{w}_a}{\mathbf{w}_a^H R_{a_v}\mathbf{w}_a} \qquad (0<|\beta_v|\leq 1). \quad (12)$$

The volume attenuation factor α_v captures the effect of the beamformer weights attenuating the volume response, such that the effective μ is increased i.e. $\mu' = \mu/\alpha_v$ and the estimator $\hat{\gamma}_{ab_g}$ of the ground coherence γ_{ab_g} is improved. β_v accounts for the differing volume coherences for non-identical passes, and may be complex because R_{ab_v} is not Hermitian. Here we analyse the simple $\beta_v = 1$ case for identical passes, and focus on controlling α_v. To suffer an estimation error of no more than 0.1, Fig. 2 indicates that the beamformer must achieve $\alpha_v = -10\,\mathrm{dB}$ if $\mu = 0\,\mathrm{dB}$ and $\alpha_v = -20\,\mathrm{dB}$ if $\mu = -10\,\mathrm{dB}$.

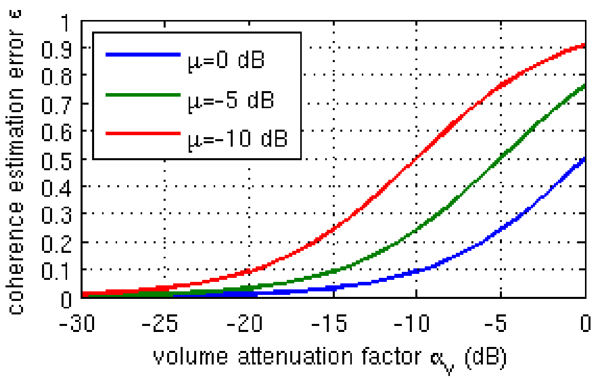

Fig. 2. Variation of the ground coherence estimation error $\epsilon = |\hat{\gamma}_{ab_g} - \gamma_{ab_g}|$ with volume attenuation factor α_v for different ground-volume power ratios μ. Here $\gamma_{ab_g} = 0$ (worst-case) and $\beta_v = 1$.

6. WEIGHT SELECTION

The beamforming weights in (11) are selected to minimise α_v and therefore the estimation error in (10). The reciprocal of (11) takes the general form $\mathbf{w}^H A\mathbf{w}/\mathbf{w}^H B\mathbf{w}$, with $A = \mathbf{1}_{N\times N}$ Hermitian and $B = R_{a_v}$ Hermitian and positive definite; $A - \lambda B$ is a regular linear matrix pencil, and it is bounded by the extreme roots (eigenvalues) of the associated characteristic equation [16]. For the case $N{=}3$ we have derived the optimum principal vector $\mathbf{w}_{opt}$ which achieves the maximum root (omitted for space), and it was found to essentially depend on the inverse of the volume-only covariance matrix $R_{a_v}^{-1}$. However, the volume-only coherences are not known or directly observed, and therefore $\mathbf{w}_{opt}$ cannot be directly implemented.

Two standard choices of weights are the conventional beamformer $\mathbf{w}_{conv} = \mathbf{v}/N$, which is used here as a reference, and the adaptive beamformer $\mathbf{w}_{mvdr}$, which uses the inverse of the observed covariance matrix R_a^{-1},

$$\mathbf{w}_{mvdr} = \frac{R_a^{-1}\mathbf{v}}{\mathbf{v}^H R_a^{-1}\mathbf{v}}. \quad (13)$$

The adaptive beamformer is the solution to the optimisation problem of minimising the output power from all heights except for the steered height (i.e. the ground), which is passed undistorted. If the SNR is not low then the volume attenuations provided by $\mathbf{w}_{opt}$ and $\mathbf{w}_{mvdr}$ are approximately equal, indicating that the practical weight selection specified by (13) is as good as can be achieved.

7. SIMULATION

Multichannel volume attenuation is now demonstrated by simulating SAR images of ground and volume clutter and displaying their coherence with and without 3D focusing to the ground. The test scenario includes rearranged ground targets to show change detection.

We synthesise data for an L-band dual-antenna radar system mounted on an airborne platform in wing pods 9 m apart – this is a configuration of the PLIS interferometer [17]. The effective phase centres will have $4.5\,\mathrm{m}$ horizontal separation. A radar bandwidth of $140\,\mathrm{MHz}$ supports ground-range Hamming-windowed resolution of $2\,\mathrm{m}$ at a nominal incidence of $\theta_0 = 45°$. At an altitude of $3000\,\mathrm{ft}$, the angular separation between channels is $\Delta\theta = 0.14°$, which puts a grating lobe at height $\lambda/(2\Delta\theta)\cos\theta_0 = 33\,\mathrm{m}$ and for which conventional beamforming would give a vertical peak-null resolution of $11\,\mathrm{m}$. The simulated scene initially contains eight $20\,\mathrm{dBsm}$ point targets $20\,\mathrm{m}$ apart on the ground, together with $0\,\mathrm{dB}$ ground and volume (2 to $5\,\mathrm{m}$ above ground) clutter. The clutter is simulated by synthesising the responses of many randomly positioned point scatterers per resolution cell; the responses are identical except for their position-dependent delay. The platform passes the scene twice, with an offset in incidence angle of $0.5°$, which allows for a typical airborne repeat-pass offset of several metres. Between passes, four targets are removed but the clutter is constant.

The sequence of images and coherence maps in Fig. 3 show that the ground coherence is moderately well-estimated after 3D MVDR beamforming, such that the changes on the ground are visible. The multichannel ($N{=}3$) processing has attenuated the volume clutter and approximately preserved the ground's complex speckle pattern. In contrast, the coherence for ordinary 2D images and 3D conventionally-beamformed images is poor due to volume decorrelation. Thus, 3D MVDR beamforming is a potentially viable processing approach. Next we consider its performance for a range of more realistic scenarios.

8. EXPONENTIAL FOREST VOLUME MODEL

Here we analyse the performance of the beamformers given a model for the volume-only coherence γ_v. Simple models have been developed and validated in the radar remote sensing literature to represent the interferometric correlation of vegetated landscapes. The widely used random-volume-over-ground (RVoG) model takes the same form as $\tilde{\gamma}_{gv}$ in (7) with $|\gamma_g|{=}1$ (we set $\phi_g{=}0$ as in Sec. 5). In this model, γ_v is the interferometric coherence of a random volume of height h_v causing exponential signal decay parameterised by extinction coefficient σ_e [18–21].

$$\gamma_v = \frac{\int_0^{h_v} e^{p_1 z} e^{jk_z z}dz}{\int_0^{h_v} e^{p_1 z}dz} = \frac{p_1(e^{p_2 h_v}-1)}{p_2(e^{p_1 h_v}-1)} = |\gamma_v|e^{j\phi_v} \quad (14)$$

where $p_1 = 2\sigma_e/\cos\theta$, $p_2 = p_1 + jk_z$ and $k_z = k_0\Delta\theta/\sin\theta$. The wavelength and collection geometry are together represented by the

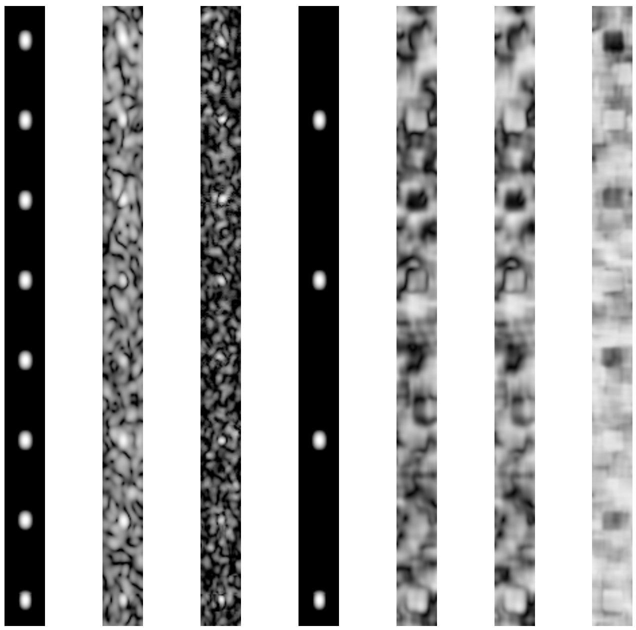

(a) initial targets (b) 2D SAR image (c) 3D MVDR image (d) changed targets (e) 2D coh. $\bar{\gamma} = 0.50$ (f) 3D conv. coh. $\bar{\gamma} = 0.55$ (g) 3D MVDR coh. $\bar{\gamma} = 0.75$

Fig. 3. Simulated 3D beamforming results (range down the page). Images (a) and (d) show the targets for the two passes without ground or volume clutter. Images (b) and (c) show the total targets+clutter scene from the first pass. (e)-(g) are coherent change maps across passes for different types of images (whiter is higher coherence), with the mean coherence in the non-target areas stated below.

vertical wavenumber k_z, which captures the net sensitivity to height. Equation (14) indicates that the entire vertical extent of the random volume appears as an effective phase centre corresponding to a single height ϕ_v/k_z above the ground surface.

Given this model, the beamformer performance can be assessed by directly populating R according to the coherence decomposition in (4) and computing α_v in (11) for selected weights. This can be repeated across the parameter space describing the radar and the scene.

Results for typical values of this forest model, shown in Fig. 4-5, indicate that the attenuation performance of the adaptive beamformer meets the approximate requirements for reasonable coherence estimation in Fig. 2. Performance can be improved by together increasing the array aperture and filling this aperture with more elements (by adding extra physical receive-only elements to increase the number of effective phase centres); changing only one of these parameters has negligible effect. Plotting the beampatterns, it was seen that the performance boost comes from the adaptive beamformer steering more nulls onto the spatially spread interference volume, but once the maximum $N-1$ nulls have been steered, changes to the array structure have little effect.

The performance is limited by the apparent nonstationarity of the volume interference, from the point of view of the beamformer. From (14), the effective phase centre of the random volume is a function of the observation geometry $\Delta\theta$, so the apparent height of the interference above the ground focus plane is different for the different channel pairs contributing to the covariance matrix – this dependence is shown in Fig. 6. Therefore, there is no single height onto which a null can be steered to remove the interference. This is a natural consequence of the spatially spread structure.

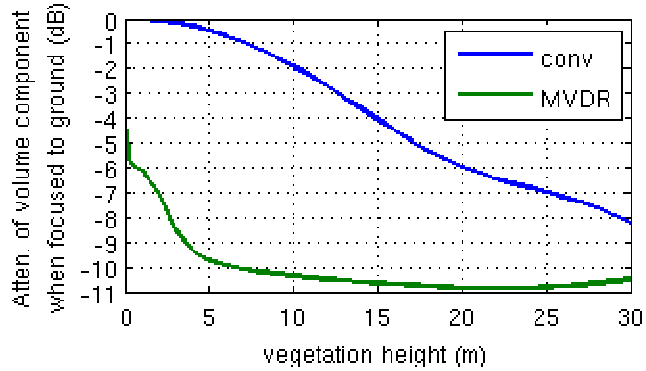

Fig. 4. Beamformer performance α_v for different vegetation heights. $N=3$, $\Delta\theta=0.1^\circ$, $\sigma_e=0.1$ dB/m, $\mu=0$ dB, $SNR = 50$ dB. For typical forest heights h_v~20 m, the MVDR beamformer achieves α_v~-10.8 dB, which is sufficient to estimate the ground coherence with error $\epsilon < 0.1$ (see Fig. 2).

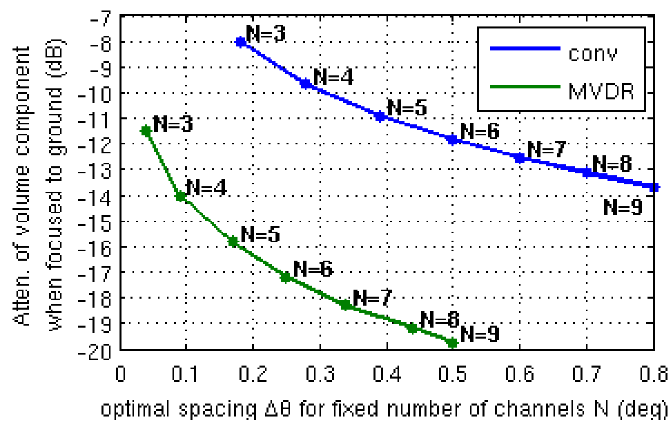

Fig. 5. Beamformer performance α_v for optimal $(N, \Delta\theta)$ combinations (optimal as in greatest attenuation). h_v=20 m, σ_e=0.1 dB/m, μ=0 dB, $SNR = 50$ dB.

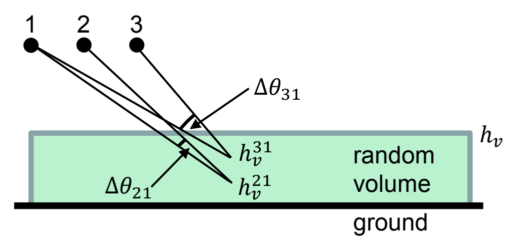

Fig. 6. RVoG scene observed by different channel pairs. The apparent height of the random volume depends on $\Delta\theta$ for each pair.

9. CONCLUSION

The results of this study indicate that 3D SAR image formation and coherent change detection of the ground under a forest canopy are achievable using data from a single-pass multichannel across-track radar system which provides at least three effective phase centres. For a canopy of typical height that can be approximated by a random volume, the adaptive beamformer steered to the ground provides in excess of 10 dB reduction in the volume contribution, permitting an improved recovery of the underlying ground coherence across passes.

10. REFERENCES

[1] G. Krieger *et al.*, "Interferometric synthetic aperture radar missions employing formation flying," *IEEE Proc.*, vol. 98, no. 5, pp. 816–843, May 2010.

[2] M. Preiss, D. A. Gray & N. J. S. Stacy, "Detecting scene changes using synthetic aperture radar interferometry," *IEEE TGRS*, vol. 44, no. 8, pp. 2041–2054, Sep. 2006.

[3] F. Lombardini, M. Montanari & F. Gini, "Reflectivity estimation for multibaseline interferometric radar imaging of layover extended sources," *IEEE TSP*, vol. 51, no. 6, pp. 1508–1519, Jun. 2003.

[4] S. Tebaldini, "Algebraic synthesis of forest scenarios from multibaseline PolInSAR data," *IEEE TGRS*, vol. 47, no. 12, pp. 4132–4142, Dec. 2009.

[5] A. Reigber & A. Moreira, "First demonstration of airborne SAR tomography using multibaseline L-band data," *IEEE TGRS*, vol. 38, no. 5, pp. 2142–2152, Sep. 2000.

[6] F. Lombardini *et al.*, "SAR tomography for scene elevation and deformation reconstruction: Algorithms and potentialities," in *Proc. Radar Conf.*, May 2008.

[7] I. Hajnsek & T. Busche, "Tandem-X: Science activities," in *Proc. EuSAR Conf.*, Jun. 2014.

[8] M. Schwäbisch *et al.*, "Early results using single-pass L-band PolInSAR," in *Proc. IGARSS*, Jul. 2008.

[9] N. J. Willis, "Bistatic radar," in *Radar Handbook*, M. I. Skolnik, Ed. McGraw-Hill, 1990.

[10] P. Lombardo & F. Lombardini, "Optimum dual-baseline SAR cross-track interferometry," in *Proc. SPIE Microwave Sensing and SAR conf.*, Sep. 1996.

[11] Q. Zhang *et al.*, "Forest height estimation using single-pass dual-baseline L-band PolInSAR data," in *Proc. IGARSS*, Jul. 2012.

[12] F. Lombardini *et al.*, "Experiments of interferometric layover solution with the three-antenna airborne AER-II SAR system," in *Proc. IGARSS*, Sep. 2004.

[13] H. A. Zebker & J. Villasenor, "Decorrelation in interferometric radar echoes," *IEEE TGRS*, vol. 30, no. 5, pp. 950–959, Sep. 1992.

[14] F. Gatelli *et al.*, "The wavenumber shift in SAR interferometry," *IEEE TGRS*, vol. 32, no. 4, pp. 855–865, Jul. 1994.

[15] C. V. Jakowatz, D. E. Wahl & D. A. Yocky, "Beamforming as a foundation for spotlight-mode SAR image formation by backprojection," in *Proc. SPIE Alg. SAR Im.*, Apr. 2008.

[16] F. R. Gantmacher, *The Theory of Matrices*. Chelsea Publishing Co. NY, 1959, vol. 1, pp. 310, 317–322.

[17] D. Gray *et al.*, "PLIS: An airborne polarimetric L-band interferometric synthetic aperture radar," in *Asia-Pacific Conf. SAR*, Sep. 2011.

[18] R. N. Treuhaft, "Vegetation characteristics and underlying topography from interferometric radar," *Radio Science*, vol. 31, no. 6, pp. 1449–1485, Nov. 1996.

[19] R. N. Treuhaft & P. R. Siqueira, "Vertical structure of vegetated land surfaces from interferometric and polarimetric radar," *Radio Science*, vol. 35, no. 1, pp. 141–177, Jan. 2000.

[20] S. Cloude, D. Corr & M. Williams, "Target detection beneath foliage using polarimetric synthetic aperture radar interferometry," *Waves in Random Media*, vol. 14, no. 2, pp. 393–414, 2004.

[21] S. Cloude, *Polarisation: Applications in Remote Sensing*. OUP, 2009, pp. 271–272.